

Influence of the Extreme Indian Ocean Dipole 2019 on the Equatorial Indian Ocean Circulation

Srinivas G^{1*}, Amol P² and Arnab Mukherjee³

¹CSIR-National Institute of Oceanography, Goa, India

²CSIR-National Institute of Oceanography, Regional Centre, Andhra Pradesh, India

³ESSO-National Centre for Polar and Ocean Research, Ministry of Earth Sciences, Goa, India

Corresponding author :Dr. Srinivas Gangiredla,

Email: srinivasg@nio.org

Abstract

This study examines direct current measurements in the central equatorial Indian Ocean during the positive phase of the extreme Indian Ocean Dipole (pIOD) in 2019. Analysis of near-surface zonal current at 77°E and 83°E reveals a notable delay in the onset of fall Wyrтки Jets (WJs), typically occurring in October. The WJs formed in December but persisted for a shorter duration. On the other hand, the subsurface currents display a strong eastward flow persistent from October 2019 to June 2020 which is abnormal to a normal condition. The anomalous subsurface zonal currents exhibited magnitudes three times stronger during pIOD 2019 compared to pIOD composites. Due to the continued sub-surface flow, wavelet analysis revealed a dominant semi-annual cycle near the surface and an annual cycle in the subsurface layers. To explore the underlying processes behind these anomalies, we used the Modular Ocean Model in conjunction with a linear, continuously stratified model. Our experiments revealed that the weakening of fall Wyrтки Jets in 2019 was driven by anomalous easterlies associated with the extreme pIOD phase. However, the persistence of eastward subsurface currents was attributed to anomalous westerlies in the western Indian Ocean. These westerlies generated Kelvin waves propagating eastward, which upon impinging the eastern boundary, reflected and propagated downwards as Rossby waves, ultimately intensifying the subsurface currents. Overall, our study underscores the significance of equatorial wave dynamics in driving currents during the extreme IOD event.

Keywords: Zonal current, Wyrтки Jets, Indian Ocean Dipole, equatorial waves, observations, ADCP.

1. Introduction

The Equatorial Indian Ocean (EIO) plays a strong role in global and regional climate change, through ocean-atmosphere-coupled processes, which also serve as a foundation for many global and regional climate and weather patterns (Saji and Yamagata, 2003). The key feature of the EIO is the robust air-sea interactions, which exhibit spatial and temporal variations from intraseasonal to interannual scales (e.g., McPhaden, 1982; Gnanaseelan et al. 2012; Gnanaseelan and Deshpande 2018). The zonal currents are the primary flow in the EIO and play a critical role in the distribution of ocean mass and heat between the western and eastern Indian Ocean (IO), thus influencing the regional weather and climate (Schott and McCreary 2001). The EIO experiences different seasonal wind forcing and is influenced by both summer and winter monsoons (Schott et al. 2009; Shankar et al. 2002). Winds over the EIO, particularly their zonal component, are weak during monsoons. In contrast, relatively strong westerly winds appear during the transition between monsoons, first during April-May (spring) and then again during October- November (fall) (Hastenrath et al. 1993). These winds drive strong eastward currents along the equator, known as Wyrtki jets (WJs; Wyrtki 1973), which transport warmer upper-layer water towards the east, causing the deeper thermocline and mixed layer and supporting a more convective atmosphere than in the west. In essence, the WJs dictate the thermocline shape in the EIO. However, the WJs are sometimes modulated due to the changes in wind patterns during specific conditions. The Indian Ocean Dipole (IOD) reflects the ocean-atmosphere systems deviation from this mean state occurring during certain years, characterized by opposite signs of anomalies in the east and west. This phenomenon is one of the dominant modes of variability of the tropical IO.

The IOD is a process that connects the ocean and atmosphere in the tropical IO and is associated with anomalous warming in the western EIO and cooling in the Eastern EIO (Saji et al. 1999; Webster et al. 1999). The IOD development is closely linked to the seasonal cycle, due to the thermodynamic air-sea feedback between an atmospheric anticyclone located to the east of Sumatra (Annamalai et al. 2003) and the ocean underneath being dependent on the seasonal cycle of winds (Li et al. 2003, Murthugudde et al. 2000). The ocean-atmosphere coupling during an IOD involves atmospheric convection, winds, SST and upper ocean dynamics. The discovery of the IOD led to the realization that the IO can have its own coupled ocean-atmosphere variations (Schott et al. 2009), rather than being entirely dependent on events in the Pacific Ocean related to El Niño Southern Oscillation (ENSO).

Several recent studies have delved into the factors behind the intense positive Indian Ocean Dipole (IOD) event that occurred in 2019. This event was the most potent IOD on record in the last

three decades in terms of both intensity and duration (Chen et al. 2023, Doi et al. 2020, Du et al. 2020). Notably, it has been revealed that the occurrence of the 2019 extreme positive IOD event featured the most significant easterly and southerly wind anomalies on record, leading to the strongest wind speed that facilitated the latent cooling to overcome the increased radiative warming over the eastern EIO, leading to unique thermodynamic forcing, as elucidated by Wang et al. (2020). Doi et al. (2020) conducted an analysis that suggested the formation of the IOD 2019 could be linked to the pre-existing El Niño in the Pacific. In particular, the first half of 2019 experienced a moderate El Niño that lasted from the autumn of 2018 (September to November) until the mid-summer of 2019 (June to July). Du et al. (2020) identified the role played by westward propagating Rossby waves, generated as a result of weak El Niño-like conditions in the Pacific, in inducing deep convection and anomalous easterly equatorial winds that triggered the initial cooling of the eastern IO during March to May. The pIOD 2019 was triggered in May by easterly wind bursts over the tropical Indian Ocean associated with the dry phase of the boreal summer intraseasonal oscillation, and it was sustained by local atmosphere-ocean interaction thereafter (Zhang et al. 2021). The quasi-stationary Madden-Julian oscillation (MJO) activity maintained over the western IO contributed to the vigorous growth of the positive IOD. Concurrently, the sustained MJO convection suppressed the precipitation anomalies triggered by the Central Pacific El Niño warming. Thus, the El Niño forcing had only a minor effect on the positive IOD 2019 and the local Bjerknes feedback contributed to it as an extreme IOD event (Huang et al. 2022). A recent study by Chen et al. (2023) suggested that the extremely positive IOD modulates the Indian Ocean circulation and, thus, regulates the basin-wide freshwater balance between the subsurface layer of the equator and the surface layer of the EIO. However, none of these studies explored the equatorial circulation response to the extreme IOD 2019, and it remains unexplored and is worth studying to comprehend the cause of ocean dynamics in generating these extreme events.

Our study focuses on investigating the relationship between extreme IOD and subsurface currents, with a specific emphasis on the peculiarities of the year 2019 and its impact on the EIO circulation. Through a set of sensitivity experiments, we aim to verify the role of anomalous westerlies in the western EIO, the developing IOD that year, and the response of equatorial currents, using a linear continuously stratified (LCS) model. Our work is organized as follows: Section 2 outlines the data used for analysis, as well as the model and experiments performed. In Section 3, we examine the observed variability of the currents from acoustic Doppler current profiler (ADCP) moorings, with a focus on the recent period. Section 4 features the results from the ocean general circulation model, along with a discussion of the main findings, and section 5 presents the LCS model experiment results. Finally, in Section 6, we summarize the key takeaways from our analysis.

2. Data and Methods

2.1 Data

We obtained observed currents from ADCPs that were placed on moorings as part of the Ocean Observation Network (OON) programme of ESSO - Indian National Centre for Ocean Information Services (INCOIS), India. These currents were measured at locations (0° , 77°E) and (0° , 83°E) between 2018 and 2021. These ADCPs allowed a near-continuous record of currents from the surface to 1400 m with a vertical resolution of 8 m and one hour's temporal sampling interval. These two moorings have two upward-looking 75 kHz ADCPs at approximately 400 and 900 m depth respectively (Jain et al. 2021). The data from the top ADCP at 83°E is missing from June 2020 to August 2021 during the study period. Deployments in the ocean are often prone to loss of data owing to fishing vandalism and instrument damage. The deep sea moorings, being entirely underwater, do not have any major data gaps due to vandalism. Yet, the missing data during this period at 83°E is due to the instrument failure. However, this would not be limited to the study of the near-surface features during the above period. The ADCP records at 77°E are continuous and they can cover the current variability in the equatorial central Indian Ocean (refer to Jain et al. 2021 for completed details about the mooring configuration and data availability). For the present study, we used the current data for the depth up to 300 m. The top 10% of these observations are not reliable due to surface backscattering that contaminates the data. Unfortunately, the lack of near-surface buoys means that useful surface current data is lost. For completeness of the analysis, we used the Modular Ocean Model (MOM) version 5.

To evaluate the model, we used the following ancillary datasets: daily currents from the Ocean Surface Current Analysis Real-time (OSCAR) product derived from satellite measurements (Bonjean and Lagerloef, 2002), monthly sea surface temperature (SST) data from the latest version of the National Oceanic and Atmospheric Administration (NOAA) Extended Reconstructed Sea Surface Temperature (ERSST v5) product (Huang et al. 2017), and daily zonal and meridional wind components at the surface level from the latest version of the European Centre for Medium Weather Forecast (ECMWF) reanalysis (ERA5) product (Hersbach et al. 2023) during the period 1990 - 2021. We utilized the Dipole Mode Index (DMI) method proposed by Saji et al. (1999) to identify IOD events. This method employs the normalized Sea Surface Temperature (SST) anomaly difference between the western EIO (50°E – 70°E and 10°S – 10°N) and eastern EIO (90°E – 110°E and 10°S – 0°N) and classifies it as an IOD event if it exceeds ± 1 standard deviation.

2.2. Ocean models

2.2.1 Modular Ocean Model

For this study, we utilized simulations from the Modular Ocean Model (MOM5) ocean general circulation model (OGCM). The model configuration is similar to Mukherjee and Ravichandran (2023). The MOM5 model has a global horizontal resolution of $0.25^\circ \times 0.25^\circ$ and 50 vertical levels with a resolution of 10m from the surface to 220m to accurately represent the upper ocean mixed layer and thermocline zones. The vertical resolution then gradually increases to a maximum thickness of 371 m at a depth of 5000 m. The K-profile parameterization (KPP) scheme was used to mix momentum and tracers vertically (Large et al. 1994). The model was given a realistic topography of 0.5° resolution derived from the 5-min global topography from ETOPO5 (Earth Topography-5 min). To account for the impact of river runoff forcing, sea surface salinity was relaxed to the monthly global climatology of Chatterjee et al. (2012) on a 60-day time scale. The MOM5 model starts with the global temperature and salinity climatology of Chatterjee et al. (2012) and is forced with CORE-II atmospheric forcing (Large and Yeager 2008), including air pressure, downward and longwave radiation, air temperature, specific humidity, precipitation, snowfall, and wind stress, at a horizontal resolution of $2^\circ \times 2^\circ$. After a climatological spin-up of 100 years, MOM5 begins using real-time atmospheric forcing from January 1979 with a horizontal resolution of $0.25^\circ \times 0.25^\circ$ and temporal resolution of 6 h from ERA5 (Wang et al. 2019). The analysis in the present manuscript focuses on model outputs from January 1990 to December 2020. We first evaluated the MOM5 model simulated currents with the OSCAR satellite product and observed ADCP currents before proceeding with analysis (Supplementary Fig. S1). The climatological mean of zonal currents from the OSCAR product displays eastward flow with a core located in the south of the equator. The seasonal cycle of zonal current in the equator indicates a strong eastward flow; Wyrki Jets (WJs), during spring (April-May) and Fall (October-November), and westward flow during summer and winter seasons. The annual mean of the currents on the equator is mainly dominated by an eastward flow driven by the WJs (Wyrki, 1973). It is noted that the model currents display a good agreement with the observation and satellite-derived products with a pattern correlation of ~ 0.82 . Thus, we proceed further with our analysis by relying on the MOM5 model simulations.

2.2.2. Linear Continuously Stratified Model (LCS)

We utilized the LCS model (McCreary et al. 1996) to comprehend the causes behind the robust equatorial subsurface circulation's response to abnormal winds during 2019. We linearized the model equations about a homogeneous density state and decomposed the variables into vertical normal modes, summing over the first 10 modes to derive the solutions. In the model configuration, we prescribed a flat bottom and realistic coastline, with a horizontal resolution of $0.25^\circ \times 0.25^\circ$ in the

domain 30°S - 30°N, 30°E - 120°E. The control (CTL) simulation was enforced with daily wind from ERA5, with a resolution of 0.25°×0.25° from 1 January 2005 to 31 December 2020 (15 years), and we used the last 10-year simulation to avoid the initialization problem. We also used the wind forcing from ASCAT satellite data, and the results were almost identical to the ERA5 wind forcing. Since the LCS model is linear, it is possible to differentiate between the local and remote forcing effects on the currents, for example, East India Coastal Currents (McCreary et al. 1996; Shankar et al. 1996). To determine the relative importance of reflected Rossby waves from the eastern boundary, we conducted a sensitivity experiment (EXP) by applying a climatological wind until July 2019 and realistic wind forcing for the remainder of the year. Thus, the experiment solution does not include waves generated by abnormal wind patterns during June and July 2019. We calculated the daily anomalies for CTL and EXP by removing daily climatology over ten years.

3. The ADCP observed current variability

This section discusses the equatorial currents observed from the ADCP mooring located at 0°, 77°E and 0°, 83°E. Figure 1 represents the time evolution of 5-day low pass filtered zonal currents from depths ranging from 50 to 300m, between 2018 and 2021. During the spring and fall seasons, the WJs, which are the primary eastward flow on the equator, are evident. A zonal current strength of 50 cm/s is utilized as the criterion for jet onset and disappearance. The spring WJ emerges in April and continues through May, reaching a depth of 150m. It manifests a strong phase of upward propagation and eventually ceases in June. The fall WJ typically appears in October and is most robust in November, starting to disintegrate in December (McCreary and Shetye, 2023). These jets are shallower and confined to 100m depth. Besides the eastward WJs, there are also westward currents between the two WJs during summer and winter, with weaker magnitudes. It is important to note that the top 10% of the ADCP records are contaminated due to strong backscattering. Therefore, surface currents are obtained from the OSCAR satellite-derived currents. The OSCAR surface currents mostly align with the observed top ADCP bin but from fall 2019 to spring 2020, an unusual behaviour in surface and subsurface currents was observed (Fig. 1b, d). The onset of fall WJs, which typically occurs in October at 77°E, was delayed by two months in 2019, forming in December but for a shorter duration (Fig. 1b, dashed vertical black line). The subsurface currents, evident from the ADCP data, persistently flowed eastwards from October 2019 to June 2020 (see supplementary Fig. S2 for zoomed view). During this period, the OSCAR currents were in the opposite direction to that of the ADCP top bin observations from February to March 2020, indicating the presence of undercurrents (Fig. 1a). At other times, the subsurface currents appear as strong current cores, with subsurface flow stronger than the surface. A similar behaviour was observed at 83°E, with a slightly higher magnitude (Fig. 1c).

Furthermore, we conducted wavelet analyses at selected depths (60m, 100m, 150m, and 250m) to investigate the dominant temporal variability of the spectra power in ADCP current observations at 77°E displayed in Figure 2. This location provided continuous current measurements during the study period. The near-surface currents at 60m depth exhibited a strong semi-annual (180-day) variability and are consistent with observations from previous studies (Wyrski 1973, Schott and McCreary, 2001, Shankar et al. 2002, Jain et al. 2021). In addition to this, there was a strong annual variability at 100m depth. The annual variability was more prominent at the subsurface, especially during summer 2019 at 150m depth and during winter 2019 at 250m depth. The strength of wave power annual variability decreased with increasing depth. In these depth ranges, the annual cycle tends to be less pronounced than the semi-annual cycle (McPhaden et al. 2015, Jain et al. 2021). However, the annual cycle is known to exhibit greater strength in the remaining parts of the north Indian Ocean (Schott and McCreary, 2001). In the following sections, we show how the anomalous westerlies in the western Indian Ocean hinder the reversal of the sub-surface currents, resulting in a weak semi-annual cycle evident in the wavelets.

In Figure 3, the time series of surface zonal current interannual anomalies averaged over the core WJs region from OSCAR currents and MOM5 OGCM are displayed. The model surface currents demonstrate a high level of agreement with OSCAR satellite currents, with a correlation coefficient of 0.8 (Fig. 3a). The interannual current anomalies showed a delay in fall WJs during 2019 for about two months, and began appearing in December for a shorter period. There was an anomalous surface westward current due to the weakening of the WJs, which was caused by the easterlies in response to pIOD (Saji et al. 1999; Vinayachandran et al. 2007). The winds associated with pIOD weakened the fall WJs (McPhaden et al. 2015). In addition, we can see the time-depth section of zonal current anomalies from ADCP observations at 77°E, which showed an anomalous eastward current persisting from fall 2019 to spring 2020 with upward phase propagation (contours, Fig. 3b). The model subsurface zonal current anomalies displayed a similar pattern with a slightly weaker magnitude. However, the seasonality and upward phase propagations are consistent with the observed anomalies, with a correlation coefficient of ~0.7 (Fig. 3b). Therefore, it is crucial to understand the evolution of anomalous subsurface currents during 2019-2020, the responsible mechanisms behind the strong currents, and their possible role in links to the extreme IOD 2019.

4 The equatorial currents response to the extreme IOD 2019

Before proceeding further, it is worthwhile to explore the strength of IOD 2019 and its evolution compared to other IOD events. Figure 4 displays the DMI from 1990-2022, with the red stars representing the IOD events (1994, 1997, 2006, 2015, 2018 and 2019) during the study period, which

occurs from September through November (the peak of IOD). Our analysis indicates that the 2019 IOD was the strongest event ever recorded in recent decades, with 3°C anomalously warming (Fig. 4a). The SST anomalies associated with IOD started to appear in June, intensify in the following months, peak in October–November, and rapidly decline thereafter (Fig. 4b). Although the 1994 and 1997 IOD events displayed similar evolution, they were co-occurred events with El Niño Southern Oscillation (ENSO). The IO equatorial subsurface circulation is largely modulated by the ENSO remote forcing and a weak contribution by the IOD forcing during the co-occurred events (Rao and Yamagata, 2004; McPhaden and Nagura, 2014). Usually, IOD develops in summer and peaks in autumn, a season leading to the peak of El Niño, and then quickly declines in winter. On the other hand, ENSO tends to develop over the eastern equatorial Pacific but peaks in the winter of the same year. However, a very strong positive IOD 2019 occurred independently of ENSO (Du et al. 2020, Lu and Ren 2020, Wang et al. 2020). Here, we present the MOM5 model simulated currents evolution during IOD composites and the extreme IOD 2019 and the associated mechanisms through internal ocean dynamics, which sheds new light on our understanding of the impact of extreme IOD 2019 on ocean circulation.

We have conducted a composite analysis using ocean model simulations to investigate the impact of IOD climate mode on equatorial current anomalies. Figure 5 depicts the monthly progression of zonal current anomalies during IOD years, encompassing the entire event from June to the following March and during the extreme IOD 2019. In August, westward surface and eastward subsurface zonal current anomalies began to manifest, which intensified from October –December, reaching a current strength of ~25 cm/s in pIOD composites. Notably, the surface westward current anomalies first emerged in eastern IO and then propagated towards the central and western IO by the end of December (Fig. 5c–g). Such behaviour is attributed to the weakening of WJs during the IOD peak (Fig. 5d–f). The anomalous westward equatorial currents are a result of a decline in eastward transport, leading to westward transport during fall. During the IOD peak, strong easterly wind anomalies prevail along the equator, exerting a significant influence on the equatorial current system (Fig. 6d–f). A similar pattern was observed in extreme IOD 2019, although the current anomalies strength was three times higher (Fig. 5m–q). The surface westward flow emerged in August from the eastern IO to the western IO and persisted in the western IO until January 2020 (Fig. 5r).

The wind stress curl anomalies associated with IOD composites and extreme IOD 2019 are depicted in Figure 6. Anomalous south-easterlies were observed in the south-eastern IO in June (0), which turned into fully established easterlies by August and reached their peak in October – November in both IOD composites (0.02 Nm^{-2}) and IOD 2019 (0.06 Nm^{-2}), with three times the magnitude (Fig.

6). These easterlies in the eastern and central IO persisted until January 2020, in contrast to the composite wind (Fig. 6q-r). The Bjerknes-like feedback process that ensued between SST anomalies and thermocline depth facilitated the rapid growth of the easterly anomalies (Cai et al. 2009). The early development of easterlies was observed in 2019, which favoured the development of an early positive IOD event by April/May aligned with SST anomalies (Fig. 4b). Strong easterly anomalies along the equator and south-easterly winds along the Sumatra/Java coast caused the downwelling Rossby wave in the southern tropical IO as a response to anomalous anticyclonic wind stress curl (Fig. 6d-f and see supplementary Fig. S3) during the developing phase of the positive IOD (Xie et al. 2002, Rao and Behera, 2005).

In the context of pIOD composites, it is noted that there exists an equatorial undercurrent that is distinguishable (contours) from the surface flow (Fig. 5d-f). The undercurrent is referred to as the subsurface current whose direction is opposite to that of the surface flow. The subsurface eastward current anomalies were established in August but reached their maximum during the IOD peak. The easterly wind anomalies along the equator drive an anomalous upwelling Kelvin wave during IOD, which radiates into the eastern IO (Fig. 6c). At the eastern boundary, these waves reflect into coastally trapped Kelvin waves and westward propagating Rossby waves (Vinayachandran et al. 2002; Rao et al. 2002). A similar pattern was observed during IOD 2019, but the propagation was three times stronger and deeper in contrast to the composites (see Supplementary Fig. S3b).

Moreover, anomalous surface eastward current anomalies were observed in June 2019 at western and central IO due to the westerly wind anomalies present there unlike in the composites (Fig. 5k, 6k). A quasi-stationary eastward propagating Madden - Julian Oscillation (MJO) activity is attributed to the anomalous westerlies in the western IO (Huang et al. 2022). These strong westerly wind anomalies in the western EIO drive an anomalous downwelling Kelvin wave, which radiates into the eastern boundary and then reflects into coastally trapped Kelvin and Rossby waves, which remotely affect sea level variations and thermal structure along the eastern EIO. The energy from the reflected Rossby waves propagates both westwards and downwards (McCreary 1984), leading to strong and persistent eastward subsurface currents during IOD 2019. This is consistent with the observed ADCP data reported in section 3.1 and the results are in line with the previous studies (Huang et al. 2018, Amol et al. 2022). The reflected downwelling Rossby wave at the eastern boundary travelled westward, deepening the isothermal layers in the western EIO. Consequently, the surface atmospheric forcing has a profound impact on the variation in the isothermal layers in both the eastern EIO and western EIO (Vinayachandran et al. 2002).

We employ the lead-lag correlation analysis to examine the dynamics of these equatorial currents. In Figure 7, we present the lead-lag correlation between the zonal current anomalies, an area-averaged (green box on Fig. 6k) westerly wind anomalies, and overlaid ray paths for both Kelvin and Rossby waves. The maximum correlation of zonal current anomalies is linked to the surface wind forcing in western IO (Fig. 7a). The ray paths for the annual cycle were plotted from the western and eastern IO, representing the Kelvin waves (blue curve) and incident Rossby waves (black curve) driven by the anomalous westerlies from the western IO (Fig. 7a-b), as well as the reflected Rossby waves (black curve) from the eastern boundary. It is essential to note that the beam path varies with the location of wind forcing, which fluctuates along the equator. The incident Kelvin wave ray path propagated downward and eastward in the upper 100m (Huang et al. 2018; Amol et al. 2022). Upon reaching the eastern boundary, it reflects into Rossby waves that propagate westward into the deeper depths. The high correlation values gradually propagate from the east toward the west and extend to deeper depths in the central IO suggesting the wave propagations downwards and westwards (Fig. 7h-j). The downward propagation of the Rossby waves at annual periods, emanating from the eastern boundary of the EIO leads to strong and persistent eastward zonal current anomalies in the subsurface. The blue box in Fig. 7 shows regions of positive correlation where the sub-surface current continues to flow eastward instead of flowing westward. During normal years the semi-annual reflected Rossby waves cause the sub-surface currents to flip direction in this region (Nagura and McPhaden, 2012; 2016).

The analysis suggests that the anomalous strong eastward flow observed in the subsurface equatorial current systems during IOD 2019 could be attributed to the westerly wind anomaly in the western IO (Fig. 6k). To isolate the impact of westerly winds on the equatorial current systems, we utilised the LCS model to separate the response of these currents to anomalous wind forcing in the western IO. This region exhibits a unique feature in IOD 2019, which underscores the importance of this study (Fig. 6a, k). Our LCS model simulations used daily winds from the ERA5 reanalysis product. Before proceeding with the model simulations, we first examined the equatorial winds during 2019, using monthly means of zonal wind mean and anomaly on the equator, which are shown in Figure 8. The absence of climatological westerlies in the central and eastern IO during the fall of 2019 caused WJs to weaken during the same period (Fig. 8c). On the other hand, persisting westerlies in the western edge of the basin starting from the summer of 2019 which is not presented in the composite winds (Fig. 8a, b), contributed to the anomalous surface eastward zonal current anomalies during June 2019 (Fig. 5k). Consequently, anomalous Kelvin waves are generated to the eastern boundary, where they are reflected as Rossby waves with downward and westward propagation (Vinayachandran et al.

2002). However, it is challenging to differentiate the effects of westerly and easterly winds in observations and OGCMs. Therefore, to ascertain the relative contribution of reflected and directly forced Rossby waves, we analysed the simulations using the LCS model. The LCS model provides an opportunity to detect the wave processes associated with subsurface currents, as the model output can be differentiated into wind-forced and boundary-reflected waves.

5. LCS model experiments

This section presents an evaluation of the wind-forced and boundary-reflected waves relative contribution to the subsurface anomalous eastward flow maintenance, using LCS model simulations. The LCS model control (CTL) simulation closely aligned with the ADCP observed features, albeit with slightly high magnitudes. The simulation exhibited persistent subsurface eastward currents from fall 2019 to spring 2020, as seen in the ADCP observations (Figure not shown). In addition, Figure 9 displays the monthly evolution of zonal current anomalies during IOD 2019. The CTL simulation accurately captured the surface westward and subsurface eastward zonal current anomalies during the IOD peak. However, the subsurface currents' magnitudes were higher than the OGCM currents and limited to shallower depths (Fig. 5f-i, 9f-i). Furthermore, the reflected Rossby wave energy propagated downward and westward, akin to OGCM currents. Ultimately, the CTL simulation featured the current variability with significant accuracy.

Our analysis showed that the unique feature of IOD 2019 the anomalous westerly wind in the western IO plays a strong role in driving the equatorial currents (Fig. 6a-b, k-l). Therefore, we performed a sensitivity experiment using the LCS model by imposing climatological wind until July 2019, followed by realistic wind forcing for the remainder of the model simulation. This experiment aimed to suppress the generation of equatorial waves during the June and July months of 2019, which are responsible for the persistent subsurface eastward currents after the peak of IOD 2019. Fig. 9 reveals a noticeable difference between the CTL and EXP simulations. The climatological winds cause the near-surface currents during June (Fig. 9k) to be in the opposite direction to that caused by the 2019 IOD winds in the CTL run (Fig. 9a). The eastward (westward) current in the western (eastern) IO is replaced by the westward (eastward) current. Notably, the LCS experiment would also modify the behaviour of the Kelvin wave and generate a weaker Rossby wave that propagates westwards and downwards from the eastern boundary. During November and December, the suppression of wind forcing from June to July primarily weakens the westward surface current and eastward sub-surface current (Fig. 9p,q). The patchy weakening or disappearance of sub-surface cores continues till March 2020 (Fig. 9r-t).

Figure 10 shows the schematic of the key processes involved in the subsurface evolution of the pIOD 2019. The shading represents the surface (subsurface) evolution of zonal current anomalies during June (October through December). The surface wind anomalies (black vectors) trigger the eastward propagating downwelling Kelvin waves (red arrow), after reaching the eastern boundary they are reflected as downward and westward propagating Rossby waves (green arrow). The analysis shows that the anomalous June-July wind, which is unique to IOD 2019, is important to maintain a persistent eastward subsurface current and strengthen the anomalous westward current associated with IOD from October to December.

6. Summary and conclusions

The paper discusses the observed current variability from recent records of ADCP mooring located at the longitudes 77° and 83°E on the equator. The zonal currents in the central IO are dominated by semi-annual variability in the near-surface and annual variability in the subsurface. ADCP observations revealed a strong and persistent eastward flow below the surface at 80 – 150 m depth from fall of 2019 to spring of 2020. An anomalous surface westward flow and subsurface eastward flow is reported during the above period. A strong positive Indian Ocean Dipole (pIOD) event with 3°C anomalous warming in the surface was recorded in 2019 which is an extreme event in the recent period (Zhang et al. 2021; Du et al. 2020). The anomalous westward flow in the surface is mainly due to the weakening of WJs during fall caused by the easterlies driven by the extreme IOD 2019. In addition to easterlies in the eastern basin, a unique feature in IOD 2019 is the anomalous westerly winds in the western IO during the early summer months. The intensified westerly winds are not exclusive to the western IO but are also observed in other basin regions, such as the southern IO or specific months in the Arabian Sea and the Bay of Bengal (Fig. 6). Currently, it remains uncertain whether these westerly enhancements result from the dynamics of the IOD or other processes. Nonetheless, the westerlies in the western IO excite incident Kelvin waves, and once they reach the eastern boundary, they are reflected as Rossby waves that propagate downward and westward as equatorial beams (McCreary, 1984; Huang et al. 2018; Amol et al. 2022). Consequently, the sub-surface currents strengthened and maintained a consistent eastward flow with a westward phase propagation. Further, we reaffirmed the dynamics responsible for the abnormal response of subsurface currents to IOD 2019 using LCS model experiments. The sensitivity experiment revealed that westerlies during the developing phase of IOD could enhance the ocean response through equatorial wave dynamics. Thus, air-sea coupled processes involved in the equatorial region are responsible for the growth of extreme IODs. Therefore, our findings advocate that the role of equatorial wave dynamics contributes to the development of strong IODs.

Acknowledgements

This work was carried out with financial support from the ESSO - INCOIS, Ministry of Earth Sciences, India via their ECO-IOD program and CSIR. The authors acknowledge Dr. Shankar D. and Dr. Aparna S.G. for helping in scientific discussions. The support from the CSIR-NIO mooring group, ship cell members, officers, crew, and seamen from various cruises is gratefully acknowledged. The mooring operations were carried out on the research vessel R. V. Sindhu Sadhana. The authors also thank V. S. N. Murty and his colleagues for overseeing the deep-sea mooring programme from 2000 to 2017. PyFerret (PMEL/NOAA) is used for analysis and graphics. This is CSIR-NIO contribution xx.

Author contributions

SG conceptualized the study, performed the analysis, and wrote the manuscript. AP and AM participated in interpreting the results, and AM performed the model. All authors contributed to the manuscript edits.

Data availability

All the datasets and model simulations in this study are available with the corresponding author provided with a valid reason.

Declaration of competing interest

The authors declare that they have no known competing financial interests or personal relationships that could have appeared to influence the work reported in this paper.

References

- Amol P, Jain V and Aparna S 2022 Blue-shifted deep ocean currents in the equatorial Indian Ocean; *Clim. Dyn.* **59** 1–11; <https://doi.org/10.1007/s00382-021-06125-9>.
- Annamalai, H., R. Murtugudde, J. Potemra, S.-P. Xie, P. Liu, and B. Wang (2003), Coupled dynamics over the Indian Ocean: Spring initiation of the zonal mode, *Deep Sea Res., Part II*, **50**, 2305–2330.
- Bonjean, F., and G. S. E. Lagerloef. 2002. Diagnostic model and analysis of the surface currents in the tropical Pacific Ocean, *American Meteorological Society*, 32.
- Cai, W., Cowan, T., & Raupach, M. (2009). Positive Indian Ocean Dipole events precondition southeast Australia bushfires. *Geophysical Research Letters*, **36**(19), L19710. <https://doi.org/10.1029/2009GL039902>
- Chatterjee A, Shankar D, Shenoi SSC, Reddy GV, Michael GS, Ravichandran M, Gopalkrishna VV, Rao EPR, Bhaskar TVSU, Sanjeevan VN (2012) A new atlas for temperature and salinity for the north Indian Ocean. *J Earth Syst Sci* 121:559–593. <https://doi.org/10.1007/s12040-012-0191-9>

- Chen, G., Han, W., Ma, X., Li, Y., Zhang, T., & Wang, D. (2023). Role of extreme Indian Ocean Dipole in regulating three-dimensional freshwater content in the Southeast Indian Ocean. *Geophysical Research Letters*, *50*, e2022GL102290. <https://doi.org/10.1029/2022GL102290>
- Chen, G., Han, W., Wang, D., Zhang, L., Chu, X., He, Y., & Chen, J. (2023). Seasonal structure and interannual variation of the South Equatorial Current in the Indian Ocean. *Journal of Geophysical Research: Oceans*, *127*, e2022JC018969. <https://doi.org/10.1029/2022JC018969>
- Doi T, Behera SK, Yamagata T (2020) Predictability of the super IOD event in 2019 and its link with El Niño Modoki. *Geophys Res Lett* 47(7). e2019GL086713
- Du Y, Zhang Y, Zhang LY, Tozuka T, Ng B, Cai W (2020) Thermocline warming-induced extreme Indian Ocean Dipole in 2019. *Geophys Res Lett* 47(18):e2020GL090079
- Gnanaseelan, C. and Deshpande, A. 2018, Equatorial Indian Ocean subsurface current variability in an Ocean General Circulation Model, *Climate Dynamics*, *50*, 1705-1717, doi:10.1007/s00382-017-3716-8.
- Gnanaseelan, C., A. Deshpande, and M. J. McPhaden (2012), Impact of Indian Ocean Dipole and El Niño/Southern Oscillation forcing on the Wyrтки jets, *J. Geophys. Res.*, **117**, C08005, doi:[10.1029/2012JC007918](https://doi.org/10.1029/2012JC007918).
- Hastenrath S, Nicklis A and Greischar L 1993 Atmospheric hydrospheric mechanisms of climate anomalies in the western equatorial Indian Ocean; *J. Geophys. Res.* **98** 20219–20235.
- Hersbach, H., Bell, B., Berrisford, P., Biavati, G., Horányi, A., Muñoz Sabater, J., Nicolas, J., Peubey, C., Radu, R., Rozum, I., Schepers, D., Simmons, A., Soci, C., Dee, D., Thépaut, J-N. (2023): ERA5 hourly data on single levels from 1940 to the present. Copernicus Climate Change Service (C3S) Climate Data Store (CDS), DOI: [10.24381/CDs.adbb2d47](https://doi.org/10.24381/CDs.adbb2d47)
- Huang K, McPhaden MJ, Wang D, Wang W, Xie Q, Chen J, Shu Y, Wang Q, Li J, Yao J (2018) Vertical propagation of mid-depth zonal currents associated with surface wind forcing in the equatorial Indian Ocean. *J Geophys Res Oceans* 123(10):7290–7307. <https://doi.org/10.1029/2018JC013977>
- Huang, B., Peter W. Thorne, et. al, 2017: Extended Reconstructed Sea Surface Temperature version 5 (ERSSTv5), Upgrades, validations, and intercomparisons. *Journal of Climate*, doi: [10.1175/JCLI-D-16-0836.1](https://doi.org/10.1175/JCLI-D-16-0836.1)
- Huang, Z., Zhang, W., Liu, C. et al. (2022). Extreme Indian Ocean dipole events associated with El Niño and Madden–Julian oscillation. *Clim Dyn* **59**, 1953–1968 <https://doi.org/10.1007/s00382-022-06190-8>
- Jain V, Amol P, Aparna S, Fernando V, Kankonkar A, Murty V, Almeida A, Sardar AA, Khalap S, Satelkar N et al (2021) Two decades of current observations in the equatorial Indian Ocean. *J Earth Syst Sci* 130(2):1–8. <https://doi.org/10.1007/s12040-021-01568-4>
- Large WG, McWilliams JC, Doney SC (1994) Oceanic vertical mixing: a review and a model with a nonlocal boundary layer parameterization. *Rev Geophys* 32(4):363–403. <https://doi.org/10.1029/94RG01872>

- Large WG, Yeager SG (2008) The global climatology of an interannually varying air–sea flux data set. *Clim Dyn* 33:341–364. <https://doi.org/10.1007/s00382-008-0441-3>
- Li, T., B. Wang, C.-P. Chang, and Y. Zhang (2003), A theory for the Indian Ocean Dipole-Zonal Mode, *J. Atmos. Sci.*, **60**, 2119–2135.
- Lu, B., & Ren, H.-L. (2020). What caused the extreme Indian Ocean Dipole event in 2019? *Geophysical Research Letters*, 47, e2020GL087768.
- McCreary J.P. and Shetye S.R. (2023) Observations and Dynamics of Circulations in the North Indian Ocean. *Atmosphere, Earth, Ocean & Space*, Springer <https://doi.org/10.1007/978-981-19-5864-9>
- McCreary JP (1984) Equatorial beams. *J Mar Res* 42(2):395–430. <https://doi.org/10.1357/002224084788502792>
- McCreary, J.P., Han, W., Shankar, D., Shetye, S.R., 1996. Dynamics of the East India coastal current: 2. Numerical solutions. *J. Geophys. Res. Oceans* 101 (C6), 13993–14010. <http://dx.doi.org/10.1029/96JC00560>
- McPhaden, M. J. (1982), Variability in the central equatorial Indian Ocean. Part I: Ocean dynamics, *J. Mar. Res.*, **40**, 157–176.
- McPhaden, M. J. and M. Nagura (2014), Indian Ocean Dipole interpreted in terms of Recharge Oscillator theory, *Clim. Dyn.*, **42**, 1569–1586. doi [10.1007/s00382-013-1765-1](https://doi.org/10.1007/s00382-013-1765-1).
- McPhaden, M. J., Wang, Y. & Ravichandran, M. (2015) Volume Transports of the Wyrtki Jets and Their Relationship to the Indian Ocean Dipole. *J. Geophys. Res.* doi: 10.1002/2015JC010901.
- Mukherjee, A., Ravichandran, M. (2023) Role of atmospheric heat fluxes and ocean advection on decadal (2000–2019) change of sea-ice in the Arctic. *Clim Dyn* **60**, 3503–3522. <https://doi.org/10.1007/s00382-022-06531-7>
- Murtugudde, R., McCreary, J. P., & Busalacchi, A. J. (2000). Oceanic processes associated with anomalous events in the Indian Ocean with relevance to 1997–1998. *Journal of Geophysical Research*, 105, 3295–3306.
- Nagura M, McPhaden MJ (2012) The dynamics of wind-driven intraseasonal variability in the equatorial Indian Ocean. *J Geophys Res Oceans*. <https://doi.org/10.1029/2011JC007405>
- Nagura M, McPhaden MJ (2016) Zonal propagation of near-surface zonal currents about surface wind forcing in the equatorial Indian Ocean. *J Phys Oceanogr* 46(12):3623–3638. <https://doi.org/10.1175/JPO-D-16-0157.1>
- Rao S A and Behera S K 2005 Subsurface influence on SST in the tropical Indian Ocean: Structure and interannual variability; *Dynam. Atmos. Ocean* **39** 103–135.
- Rao S A, Behera S K, Masumoto Y and Yamagata T 2002 Interannual subsurface variability in the tropical Indian Ocean with a special emphasis on the Indian Ocean dipole; *Deep-Sea Res. Part II* **49** 1549–1572.

- Rao, S. A., and T. Yamagata, 2004: Abrupt termination of Indian Ocean dipole events in response to intraseasonal disturbances. *Geophys. Res. Lett.*, **31** .L19306, doi:10.1029/2004GL020842.
- Saji, N. H., and T. Yamagata, 2003: Possible impacts of Indian Ocean dipole mode events on global climate. *Climate Research*, **25**, 151–169.
- Saji, N., Goswami, B., Vinayachandran, P., & Yamagata, T. (1999). A dipole mode in the tropical Indian Ocean. *Nature*, **401**, 360–363.
- Schott F A, Xie S P and McCreary J 2009 Indian Ocean circulation and climate variability; *Rev. Geophys.* **47** RG1002 doi:10.1029/2007RG000245.
- Schott F A and McCreary J P 2001 The monsoon circulation of the Indian Ocean; *Progr. Oceanogr.* **51** 1–123, [https://doi.org/10.1016/S0079-6611\(01\)00083-0](https://doi.org/10.1016/S0079-6611(01)00083-0).
- Shankar D, McCreary JP, Han W, Shetye SR (1996) Dynamics of the East India Coastal Current 1. Analytic solutions forced by interior Ekman pumping and local alongshore winds. *J Geophys Res* 101:13,975–13,991
- Shankar D, Vinayachandran P N and Unnikrishnan A S 2002 The monsoon currents in the north Indian Ocean; *Progr. Oceanogr.* **52** 63–120, [https://doi.org/10.1016/S0079-6611\(02\)00024-1](https://doi.org/10.1016/S0079-6611(02)00024-1).
- Vinayachandran P N, Iizuka S and Yamagata T 2002 Indian Ocean dipole mode events in an ocean general circulation model; *Deep-Sea Res. Part II* **49** 1573–1596.
- Vinayachandran P N, Saji N H and Yamagata T 1999 Response of the equatorial Indian Ocean to an anomalous wind event during 1994; *Geophys. Res. Lett.* **26** 1613–1615.
- Vinayachandran, P. N., Kurian, J. & Neema, C. P. (2007) Indian Ocean response to anomalous conditions in 2006. *Geophys. Res. Lett.* **34**, L15602, doi: 10.1029/2007GL030194
- Wang C, Graham RM, Wang K, Gerland S, Granskog MA (2019) Comparison of ERA5 and ERA-Interim near-surface air temperature, snowfall and precipitation over Arctic sea ice: effects on sea ice thermodynamics and evolution. *Cryosphere* 13:1661–1679. <https://doi.org/10.5194/tc-13-1661-2019>
- Wang, G.; Cai, W.; Yang, K.; Santoso, A.; Yamagata, T. A **2020** Unique Feature of the 2019 Extreme Positive Indian Ocean Dipole Event. *Geophys. Res. Lett.*, **47**, e2020GL088615
- Webster, P. J., Moore, A. M., Loschnigg, J. P. and Leben, R. R., 1999, Coupled oceanic-atmospheric dynamics in the Indian Ocean during 1997-98, *Nature*, **401**, 356-360, World Scientific Publication Company, Singapore
- Wyrtki K 1973 An equatorial jet in the Indian Ocean; *Science* **181** 262–264.
- Xie S P, Annamalai H, Schott F A and McCreary J P 2002 Structure and mechanisms of south Indian Ocean Climate Variability; *J. Climate* **15** 867–878.
- Zhang, L., Han, W., Hu, Z.Z., 2021. Interbasin and multiple-time-scale interactions in generating the 2019 extreme Indian Ocean Dipole. *J. Clim.* **34** (11), 4553–4566. <https://doi.org/10.1175/JCLI-D-20-0760.1>.

Figures

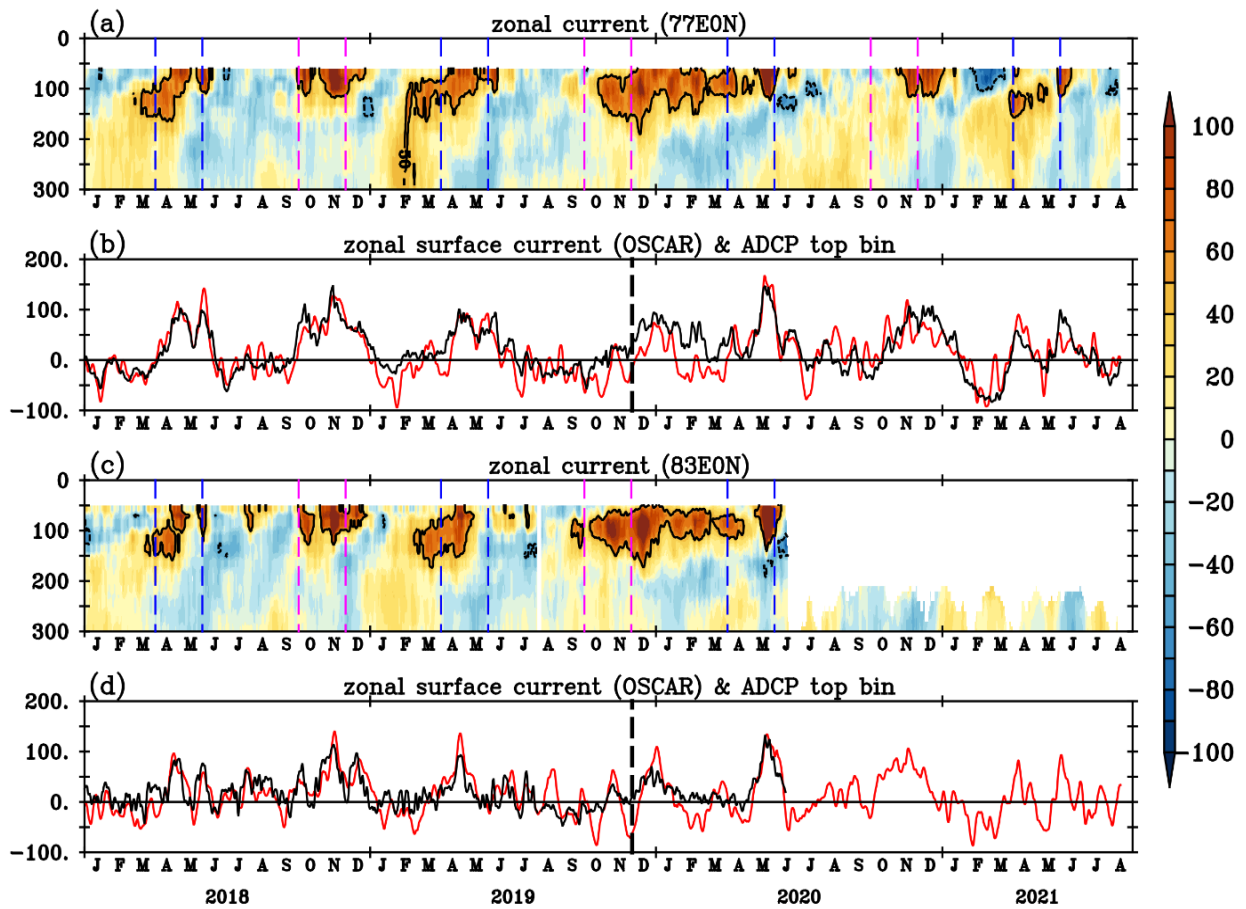


Fig. 1 Time-depth sections of 5-day low-pass filtered zonal current (cm/s) observed at (a) 0° , 77°E , and (c) 0° , 83°E from ADCP observations. Time series of 5-day low-pass filtered observed surface zonal current from OSCAR (red curve) and the top ADCP bin (black curve) at (b) 0° , 77°E , and (d) 0° , 83°E . The contour (50 cm/s) on the panel (a) and (c) show the strength of Wyrтки Jets. The dashed vertical blue (magenta) lines on panels a and c indicate the duration of Spring (Fall) Wyrтки Jets from April to May (October to November). The vertical dashed black line on panels b and d shows the delayed WJs during Fall 2019.

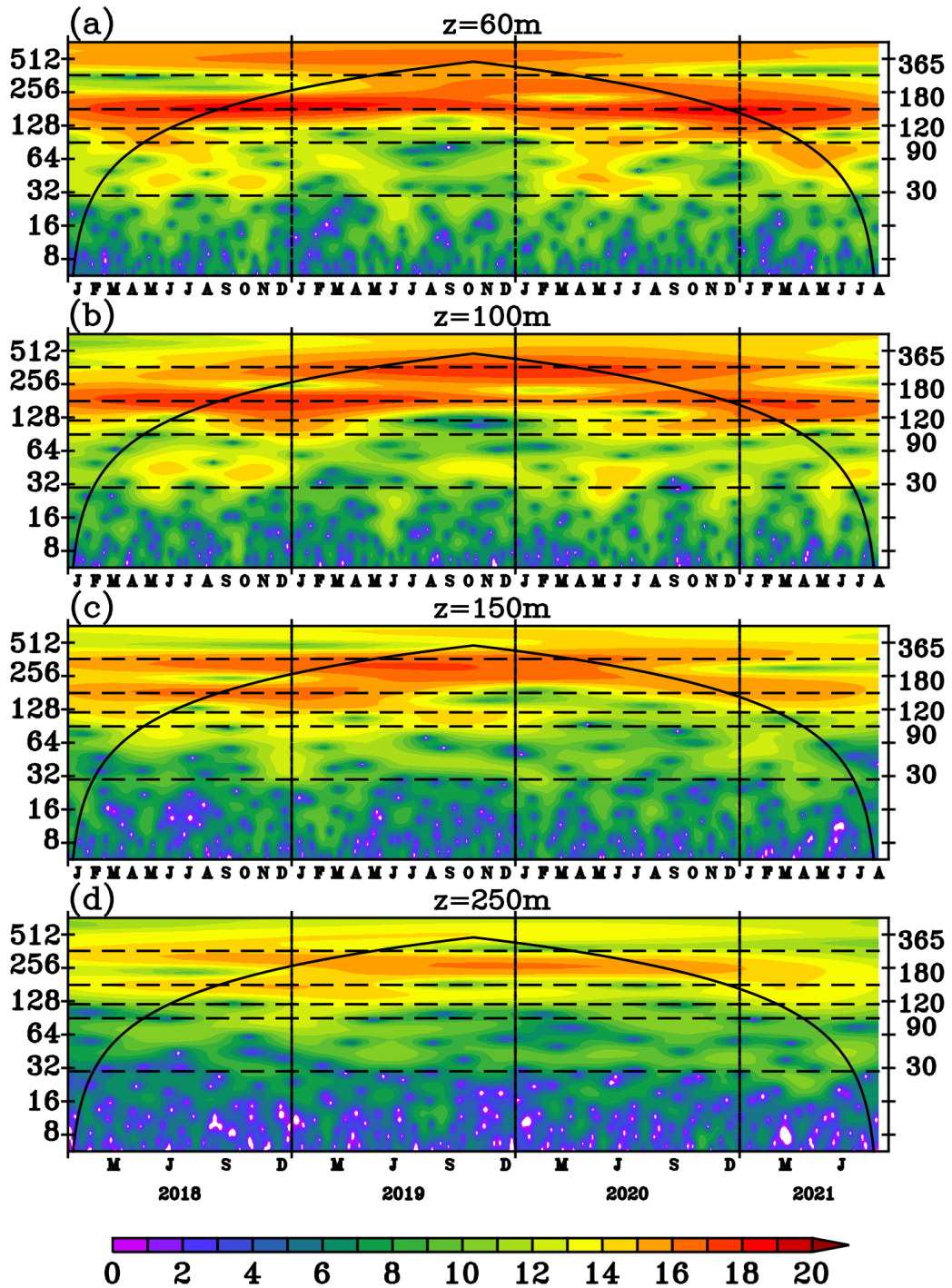


Fig. 2 Morlet wavelet spectrum of observed zonal current at 77°E , 0° from (a) 60 m (the top ADCP bin), (b) 100 m, (c) 150 m and (d) 250 m depths. The thick black line marks the cone of influence for the wavelet power spectra. The horizontal dashed lines mark the 30, 90, 120, 180 and 365-day periods.

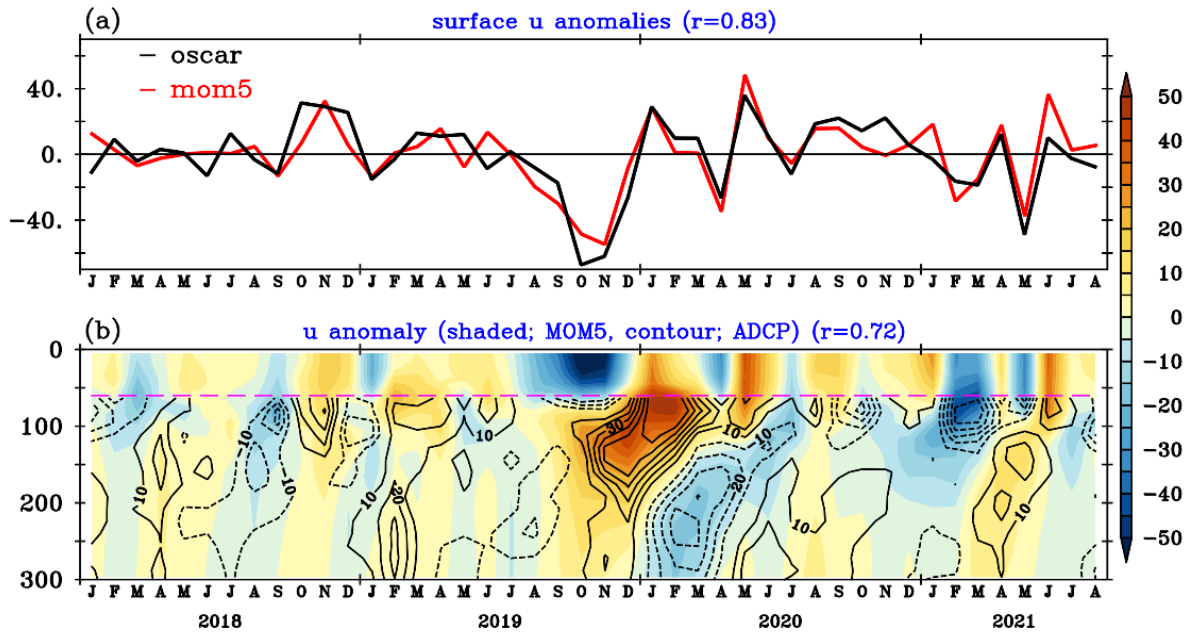


Fig. 3 (a) The interannual anomalies of surface zonal current (cm/s; average of 75° - 85° E on the equator) from OSCAR (red curve) and MOM5 model (black curve). (b) Time-depth sections of zonal current anomalies from the MOM5 model (shaded, cm/s) and ADCP observations (contours, cm/s) at 0° , 77° E. The horizontal dashed magenta lines on panel b show the corresponding depth of the top ADCP bin (60m).

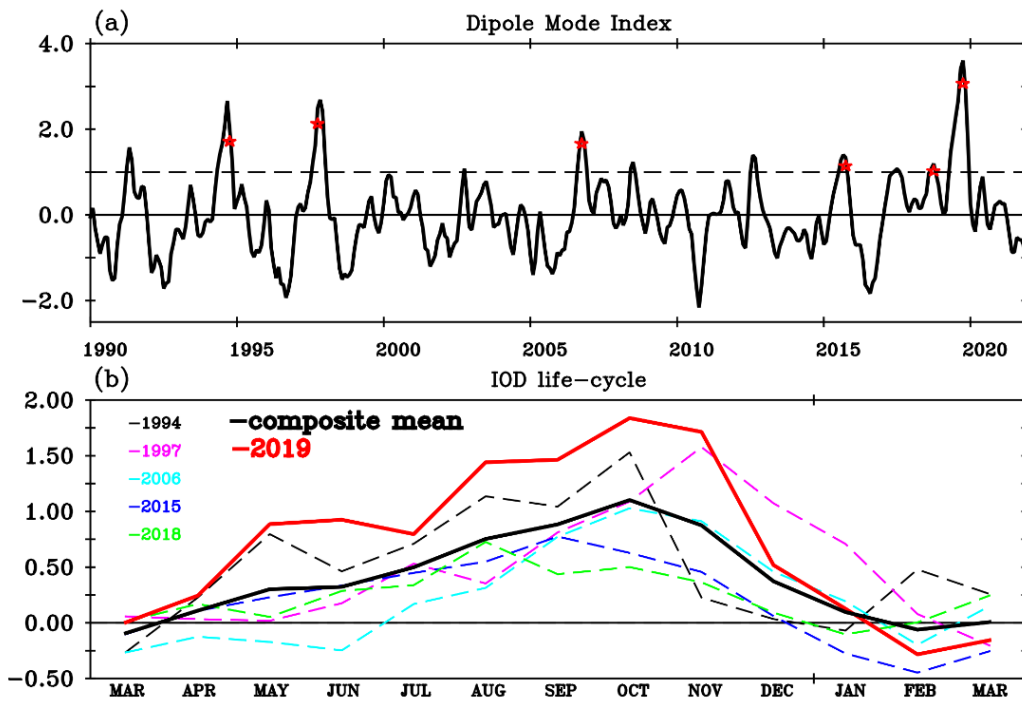


Fig. 4 (a) Dipole Mode Index (DMI) calculated as the normalized SST (ERSSTv5 product) anomaly difference between western IO ($50^{\circ} - 70^{\circ}\text{E}$, $10^{\circ}\text{S} - 10^{\circ}\text{N}$) and eastern IO ($90^{\circ} - 110^{\circ}\text{E}$, $10^{\circ}\text{S} - 0^{\circ}\text{N}$) during 1990-2021 and the events identified as positive Indian Ocean Dipole (pIOD) if it exceeds +1 STD (dashed black line) during September to November (SON) marked as red stars. (b) The life-cycle of selected pIOD events.

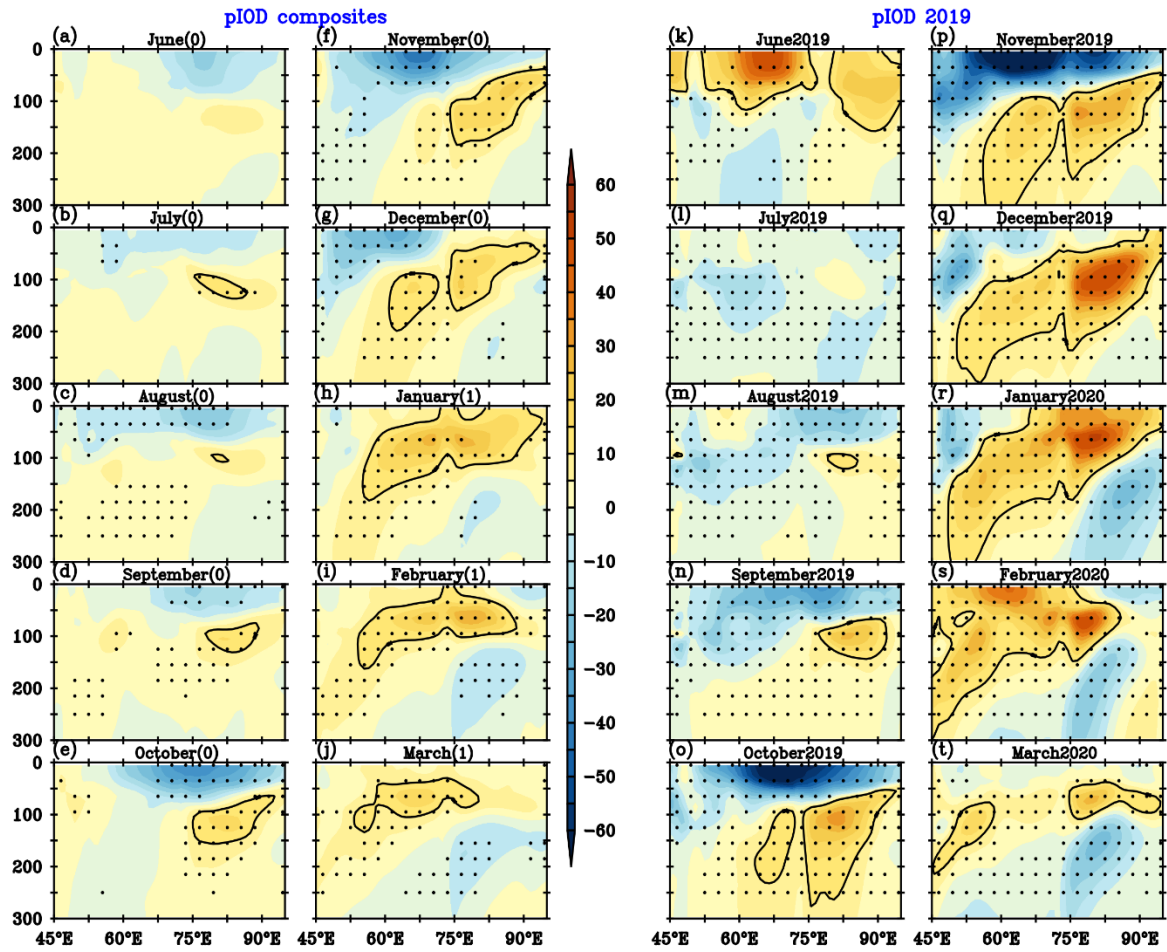


Fig. 5 Longitude-depth section of zonal current anomalies (cm/s) from MOM5 model during June (0) – March (1) for (a) - (j) pIOD composites and (k) – (t) pIOD 2019 respectively. Here (0) represents the IOD developing year and (1) is the IOD decaying year. Stippling indicates the significance at a 95% confidence level. The contours show the eastward propagation of the subsurface current anomalies.

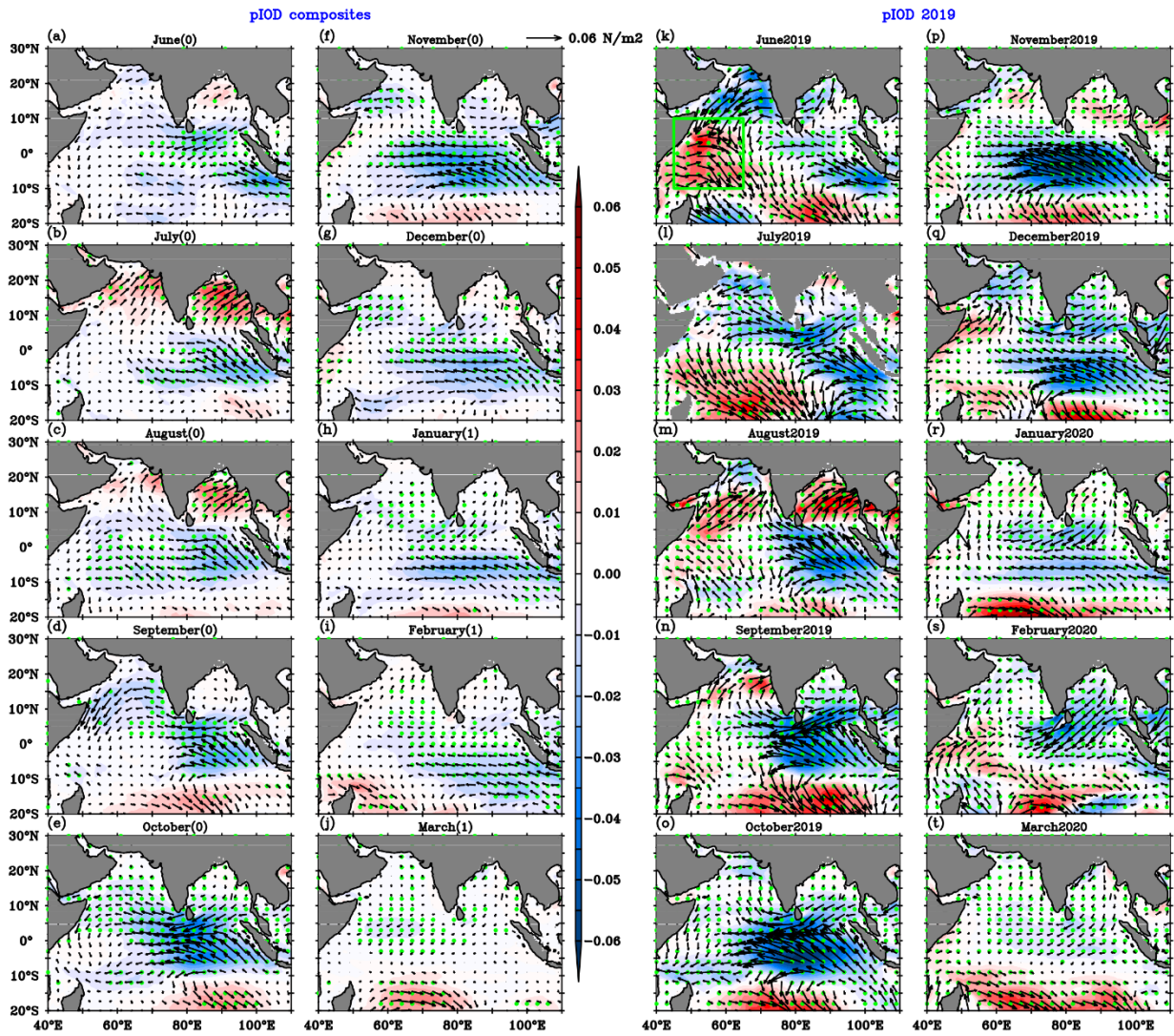


Fig. 6 The spatial maps of surface wind stress anomalies (N/m^2) from ERA5 during June (0) – March (1) for (a) - (j) pIOD composites and (k) – (t) pIOD 2019 respectively. The green box ($45 - 65^\circ\text{E}$, $10^\circ\text{S} - 10^\circ\text{N}$) indicates the anomalous westerlies during IOD 2019. Green stippling indicates the significance at a 95% confidence level.

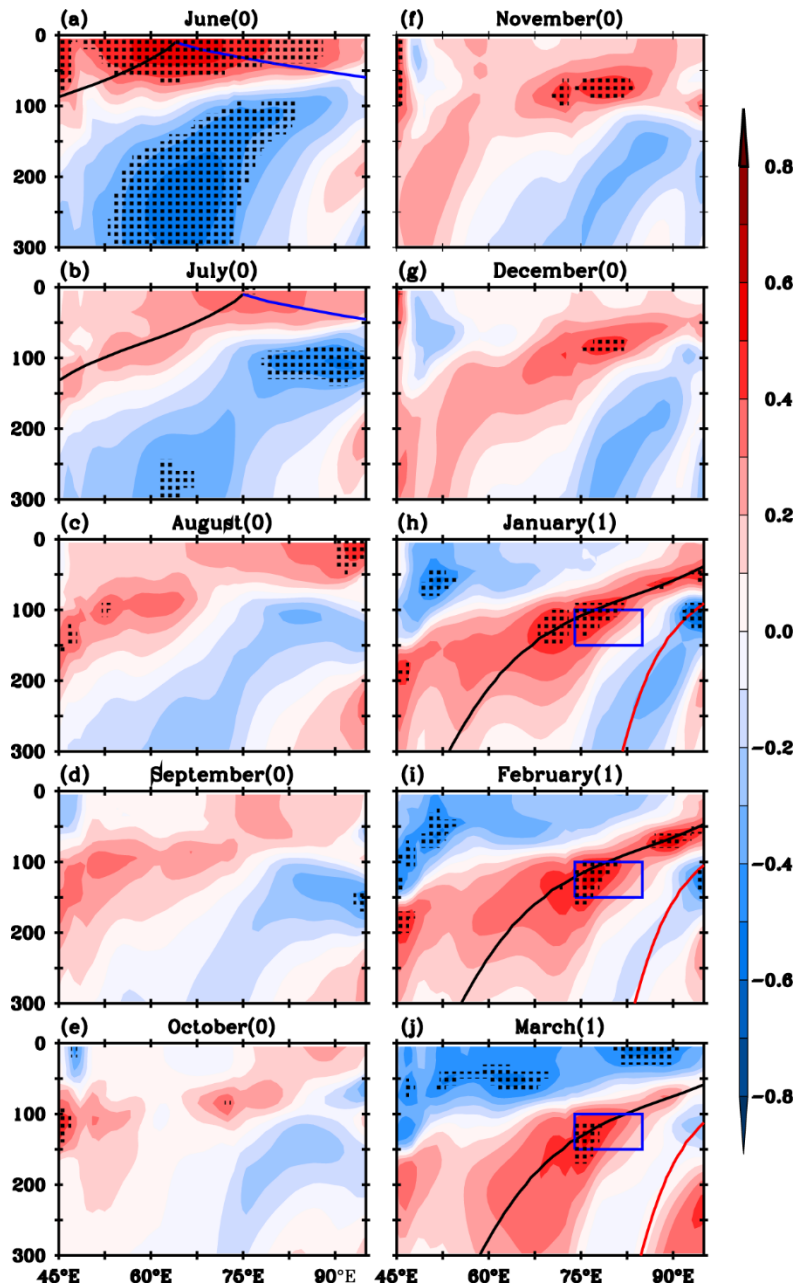


Fig. 7 The lead-lag correlation between the surface zonal wind stress anomalies (green box on fig. 6k) and zonal current anomalies from the MOM5 model during (a) – (j) June (0) to March (1). The 360-day ray paths for the Kelvin wave (blue) and the first meridional mode Rossby waves (black) are shown in panels (a)-(b) and (h)-(j). The slope of the ray paths is calculated based on Wentzel–Kramers–Brillouin (WKB) approximation and is $-\omega_0/N_b(z)$ for the Kelvin wave and $(2n + 1) \omega_0/N_b(z)$ for the n^{th} meridional-mode Rossby wave, where ω_0 denotes the frequency of the wave and $N_b(z)$ the background Brünt–Väisälä frequency profile. The blue box in panels (h)-(j) encloses the region containing the two ADCP moorings where the subsurface current does not reverse direction leading to a strong annual cycle evident in the wavelets in Figure 2(b)-(c). Stippling indicates the correlation significance at a 99% confidence level.

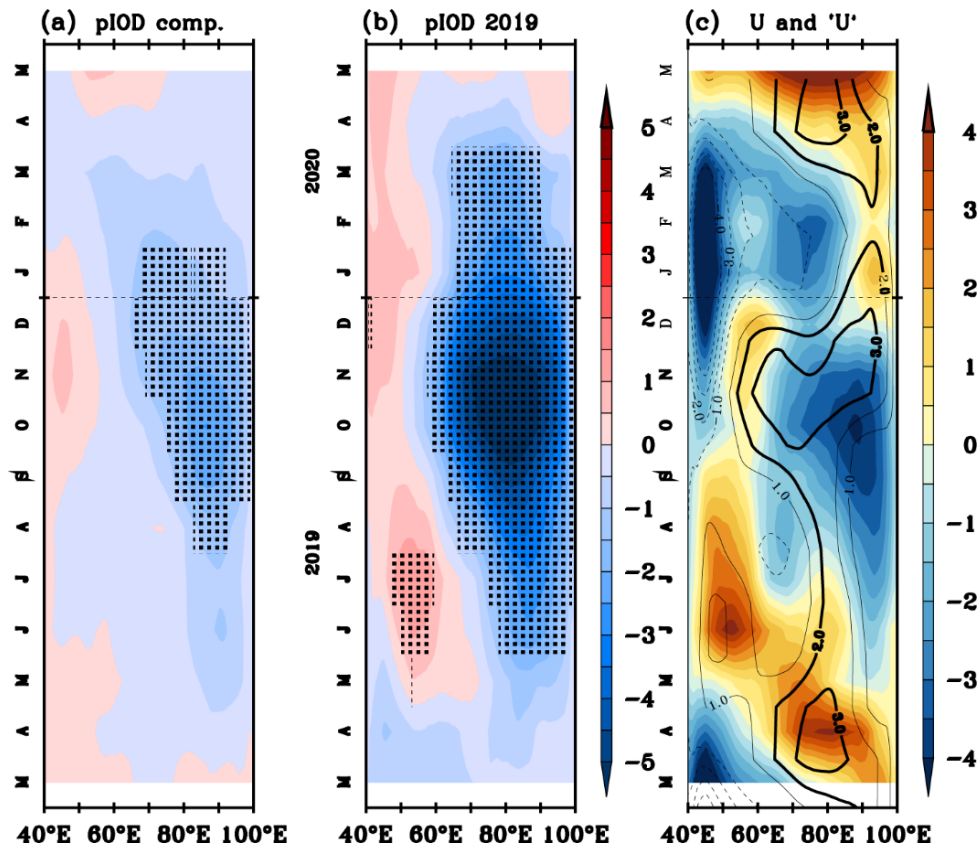


Fig 8 The Hovmöller diagram of surface zonal wind component (a) anomalies during pIOD composites and (b) pIOD 2019 event, and the mean wind during (c) 2019 (shaded) along with the climatological (contour) seasonal cycle calculated over the period 2005 – 2020. Stippling on panels a and b shows the significance at a 95% confidence level.

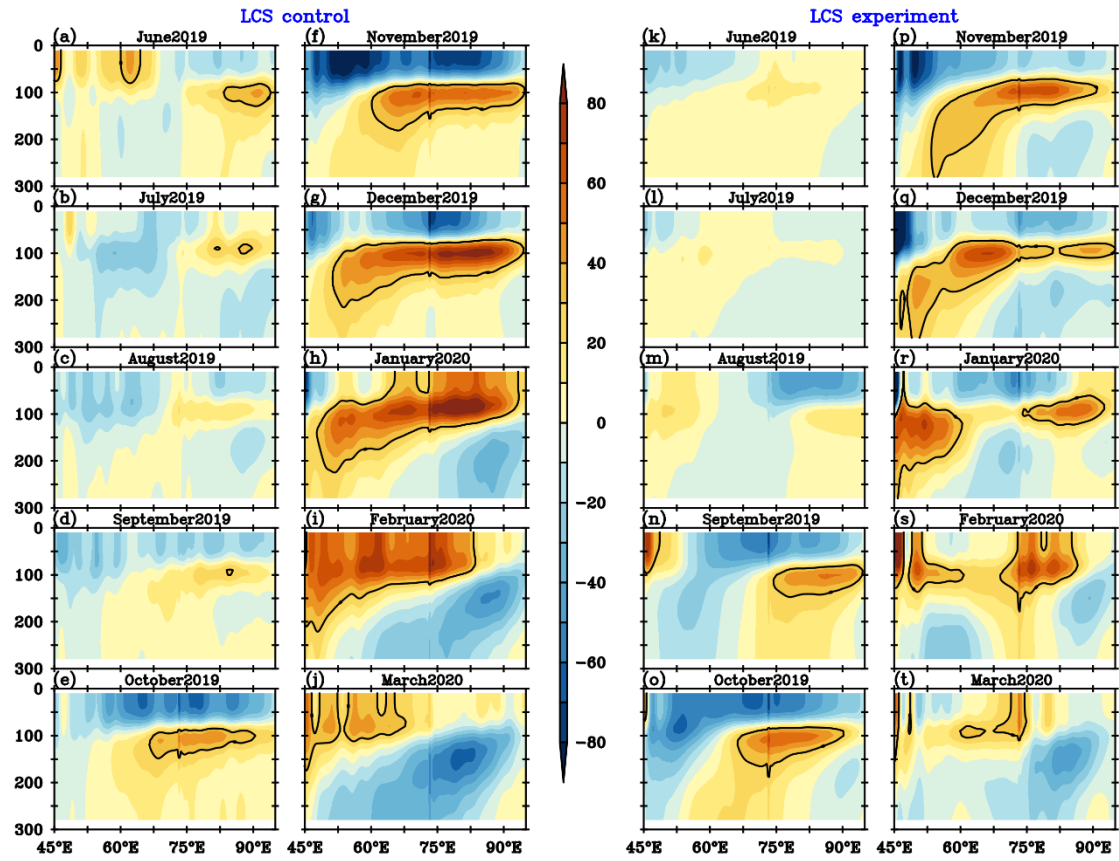


Fig. 9 Longitude-depth section of zonal current (cm/s) anomalies from June 2019 to March 2020 from (a) – (j) the LCS control and (k) – (t) experimental simulations respectively. See methods for the details of LCS model configuration and experiment design. The contours show the subsurface eastward propagations of current anomalies.

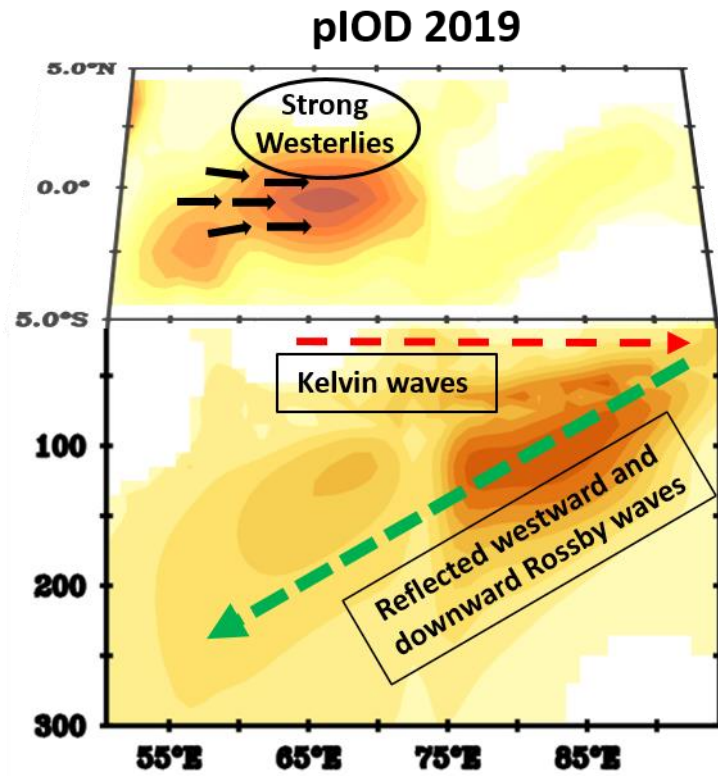


Fig. 10. Schematic of key oceanic processes of the positive IOD 2019. The surface black vectors represent the equatorial westerlies during June 2019. The colour shading shows the zonal surface (subsurface) current anomalies during June (peak of IOD). The red arrow shows the eastward propagating Kelvin waves and the green is the westward and downward propagating Rossby waves.